Tectonophysics 869 (2023) 230139

Contents lists available at ScienceDirect

Tectonophysics

journal homepage: www.elsevier.com/locate/tecto

Stress drop variations of the 2019 M_L 6.0 Changning earthquake and its aftershock sequence in the southern Sichuan Basin, China

Lin Shen [a,b], Lian-Feng Zhao [a,c,*], Xiao-Bi Xie [d], Xi He [a], Wei-Min Wang [e], Zhen-Xing Yao [a]

[a] Key Laboratory of Earth and Planetary Physics, Institute of Geology and Geophysics, Chinese Academy of Sciences, Beijing, China
[b] College of Earth and Planetary Sciences, University of Chinese Academy of Sciences, Beijing 100049, China
[c] Heilongjiang Mohe Observatory of Geophysics, Institute of Geology and Geophysics, Chinese Academy of Sciences, Beijing 100029, China
[d] Institute of Geophysics and Planetary Physics, University of California, Santa Cruz, CA 95064, USA
[e] Key Laboratory of Continental Collision and Plateau Uplift, Institute of Tibetan Plateau Research, Chinese Academy of Sciences, Beijing, China

ARTICLE INFO

Keywords:
Asia
Earthquake source observations
Induced seismicity
Joint inversion
Seismicity and tectonics
Site effects
Guided waves

ABSTRACT

The Lg-wave spectra are investigated for the 2019 Changning M_L 6.0 earthquake and its 94 aftershocks with magnitudes above M_L 2.8, which occurred in the southern Sichuan Basin, Southwest China. This earthquake sequence is potentially related to the water injection from nearby salt mining activities. Based on an established regional high-resolution broadband Lg-wave attenuation model, we correct the observed spectra for the attenuation effect along the propagation path. By fitting the observed spectra from the Changning earthquake sequence with the theoretical source model, we estimate seismic moments and corner frequencies, from which the stress drops are calculated for the entire earthquake sequence. The results show that the stress drops are rather scattered, ranging from 0.16 MPa to 32 MPa with a median value of 0.78 MPa. Spatiotemporal variation of stress drops reflects strong fault heterogeneity and a complex stress release process, which is likely influenced by water injection and diffusion. Positive trends are observed between the stress drop and focal depth and between the stress drop and seismic magnitude. Relatively lower stress drops for most shallow events are possibly the indication of lowered normal stress by long-term fluid injection. No apparent relation is observed between the stress drop and the distance to the Shuanghe salt mine, where water was injected. Combining the actual water injection data and previous numerical simulation studies, we suggest that the salt mining-related water injection may lead to elevated pore pressure beyond the source region of the 2019 Changning earthquake. The increasingly cumulated underground water may have created pathways linking multiple fault systems, thus the possibility of future large induced-earthquakes cannot be ruled out.

1. Introduction

According to the China Earthquake Networks Center (CENC), an earthquake with a local magnitude M_L 6.0 and a centroid depth of about 3 km occurred at 28.34°N, 104.90°E in Changning in the southern Sichuan Basin, China, at 22:55 local time (14: 55 UTC) on 2019 June 17 (Fig. 1) (e.g., Lei et al., 2019b; Yi et al., 2019). Following this earthquake, a series of aftershocks occurred in neighboring areas, spreading for approximately 20 km along with an orientation of 305°. As of 2019 September 30, 94 aftershocks with magnitudes greater than M_L 2.8 were recorded by the regional network, including 5 strong events with magnitudes >5, 11 events with magnitudes between 5 and 4, 64 events with magnitudes between 4 and 3, and 14 events with magnitudes between 3 and 2.8 (http://www.ceic.ac.cn/speedsearch?time=7). The epicentral area is characterized by complicated fold structures and faults of various scales and strikes (e.g., He et al., 2019; Long et al., 2020). The hypocenter relocation analysis suggested that the mainshock and major aftershocks were related to the complex Changning-Shuanghe anticlines and had generally shallow focal depths ranging from 0 to 10 km (e.g., Long et al., 2020; Yi et al., 2019). Regional velocity tomography and epicenter relocation analyses revealed that the 2019 Changning sequence was mostly related to high-velocity regions in the heterogeneous upper crust (Long et al., 2020; Zhang et al., 2013). The focal mechanism solutions for the mainshock exhibited a general thrust and strike-slip faulting, with slight differences among studies probably related to the complicated local tectonics and complex rupture process.

* Corresponding author at: Key Laboratory of Earth and Planetary Physics, Institute of Geology and Geophysics, Chinese Academy of Sciences, 19 Beituchengxilu, Chaoyang District, Beijing 100029, China.
E-mail addresses: shenlin@mail.iggcas.ac.cn (L. Shen), zhaolf@mail.iggcas.ac.cn (L.-F. Zhao), xxie@ustc.edu (X.-B. Xie), wangwm@itpcas.ac.cn (W.-M. Wang).

https://doi.org/10.1016/j.tecto.2023.230139
Received 1 June 2022; Received in revised form 14 July 2023; Accepted 14 November 2023
Available online 19 November 2023

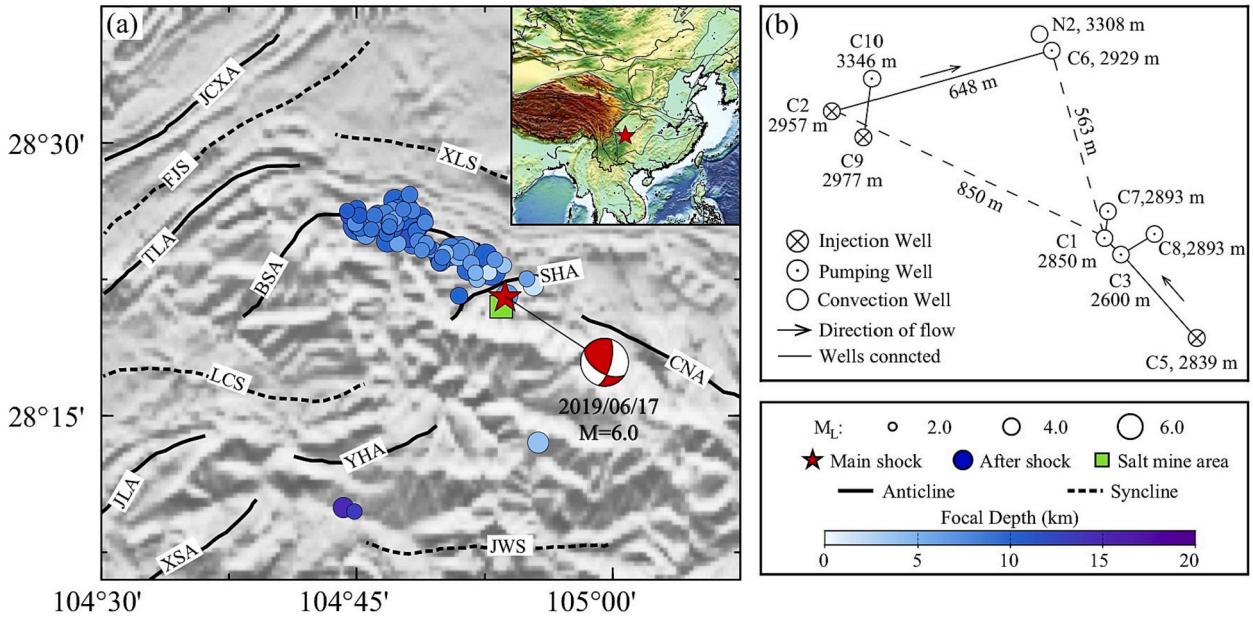

Fig. 1. (a) Map showing the locations of the 2019 June 17 Changning M_L 6.0 earthquake (star) and its aftershock sequence (blue circles). The sizes of circles are proportional to the magnitudes. The focal mechanism solution of the mainshock is indicated by the red beach ball from Lei et al. (2019b). The green square represents the Changning salt mining area. The gray-scale background image denotes the topography. (b) Spatial distribution of injection/pumping wells for salt mining labeled with IDs and depths (Sun et al., 2017). The abbreviations are BSA, Baixiangyan-Shizitan anticline; CNA, Changning anticline; FJS, Fujiang syncline; JCXA, Jiacunxi anticline; JLA, Junlian anticline; JWS, Jianwu syncline; LCS, Luochang syncline; SHA, Shuanghe anticline; XLS, Xiangling syncline; XSA, Xunsichang anticline; YHA, Yuhe anticline. (For interpretation of the references to colour in this figure legend, the reader is referred to the web version of this article.)

Liu and Zahradník (2020) suggested that the mainshock was composed of two subevents, including a motion on a thrust fault favorably oriented relative to the stress field as the site of initial nucleation, followed by a strike-slip event, which was probably facilitated by the pre-existing elevated pore pressure. Similar to the mainshock, the focal mechanisms of most aftershocks are thrust faulting, which is presumably associated with the steeply dipping thrust faults aligned along the anticlinal structure (Liu and Zahradník, 2020; Qian and Tang, 1992). By analyzing focal mechanism solutions of the main and aftershocks, Yi et al. (2019) suggested the Changning earthquake sequence is controlled by a NE-SW compressional and a NW-SE extensional deformation structure.

The 2019 Changning earthquake is the first event with a magnitude up to 6.0 in the southern Sichuan Basin (Yi et al., 2019) since the seismic record. As a stable block with a low strain rate, historically, the Sichuan Basin is characterized by low seismicity, despite the complicated small-scale fault systems observed at the surface. However, the seismicity in the southern Sichuan Basin has increased dramatically in the past few decades, possibly due to long-term water injection associated with deep-well salt mining (Ruan et al., 2008; Sun et al., 2017), recent shale gas hydraulic fracturing (Lei et al., 2017; Lei et al., 2019a; Lei et al., 2019b), and disposal of wastewater (e.g., Lei et al., 2020). The pore-pressure perturbations caused by fluid injection could reduce the frictional strength of faults, resulting in the movement of pre-existing faults which are favorably oriented in the tectonic stress field (Ellsworth, 2013; Huang et al., 2017). As typical examples, 2018 M_L 5.7 and 2019 M_L 5.3 earthquakes, which occurred ~30 km southeast of the 2019 Changning earthquake, are considered to be induced by hydraulic fracturing for shale gas (Lei et al., 2019a). Therefore, with the increasing seismicity in this region, it is urgent to monitor the induced earthquakes to reduce or avoid the potential risks from water injection activities. A fundamental solution to this issue is to identify physical similarities or differences between induced and tectonic earthquakes, especially for their source parameters, such as focal mechanisms and stress drops (e.g., Clerc et al., 2016). The stress drops can sometimes be used in discriminating the induced earthquakes from the background seismicity. The stress drop, defined as the average difference between the shear stress on the fault before and after an earthquake, is one of the fundamental parameters for predicting the ground motion (e.g., Oth, 2013; Shearer et al., 2006). For the induced earthquakes in Prague, Oklahoma, the stress drops were observed lower than those of typical tectonic earthquakes, possibly resulting from the effective normal stress that was reduced by fluid injection (Sumy et al., 2017). On the contrary, there were still arguments that the stress drops of induced and tectonic earthquakes in the central United States and western Canada are indistinguishable, suggesting that induced earthquakes, although triggered by fluid injections, were still driven by tectonic stresses (Huang et al., 2017; Wang et al., 2020). In this study, we investigate the stress drops of potential induced earthquakes in the Changning area and characterize the induced earthquakes in this region.

Since the size of the source cannot be directly observed, the stress drop is usually measured based on the seismic moment and corner frequency from the source spectrum in seismic approaches (e.g., Abercrombie, 2014; Allmann and Shearer, 2009). To determine the source spectrum of an earthquake and to estimate the stress drop, the effects of both the propagation path and site responses need to be effectively removed from the observed spectrum (e.g., He et al., 2020; Shearer et al., 2006). The empirical Green's function method is effective in removing the attenuation effect by deconvolving the observed spectrum with the spectra of nearby smaller events (Hough, 1997). Optimization methods were also used to robustly obtain the source spectrum based on the empirical Green's function. For example, an iterative least-squares stacking approach was applied to separate the source term from attenuation effects by using seismograms from overlapping source-receiver pairs (Allmann and Shearer, 2007; Shearer et al., 2006; Warren and Shearer, 2000). When the high-resolution broadband regional attenuation model is available, the attenuation effects along the propagation path can be directly calculated and used to reliably correct the source spectra (e.g., He et al., 2023; He et al., 2020). Such a strategy is often applied in magnitude measurements and explosion yield estimations (e.g., Nuttli, 1973; Nuttli, 1986; Zhao et al., 2017).

The Lg wave is one of the most prominent seismic phases in regional

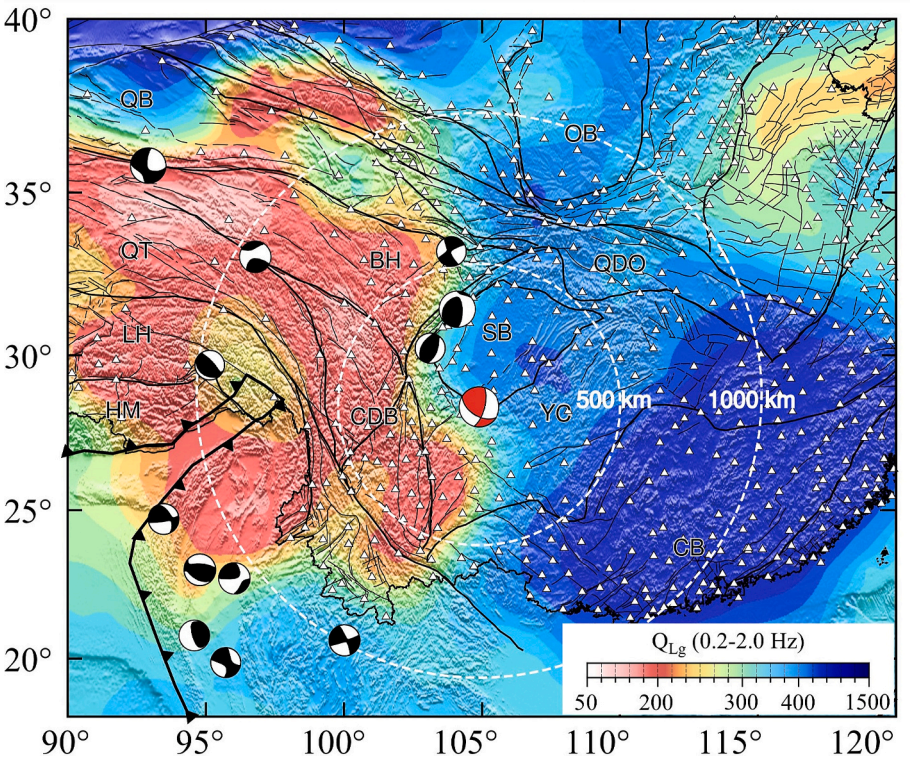

Fig. 2. The map of the broadband (0.2–2.0 Hz) regional Lg-wave Q (Zhao et al., 2013a), overlain with nearby large earthquakes greater than M_L 6.5, locations of faults, geological sutures (black lines), and seismic stations (triangles). The focal mechanisms of the nearby earthquakes (black beach ball) were from the GCMT (http://www.globalcmt.org). The abbreviations are HM, Himalaya; LH, Lhasa; QT, Qiangtang; QB, Qaidam Basin; BH, Bayan Har Block; OB, Ordos Basin; QDO, Qingling–Dabie Orogeny; SB, Sichuan Basin; YC, Yangtze Craton; CDB, Chuandian Block; and CB, Cathaysia Block.

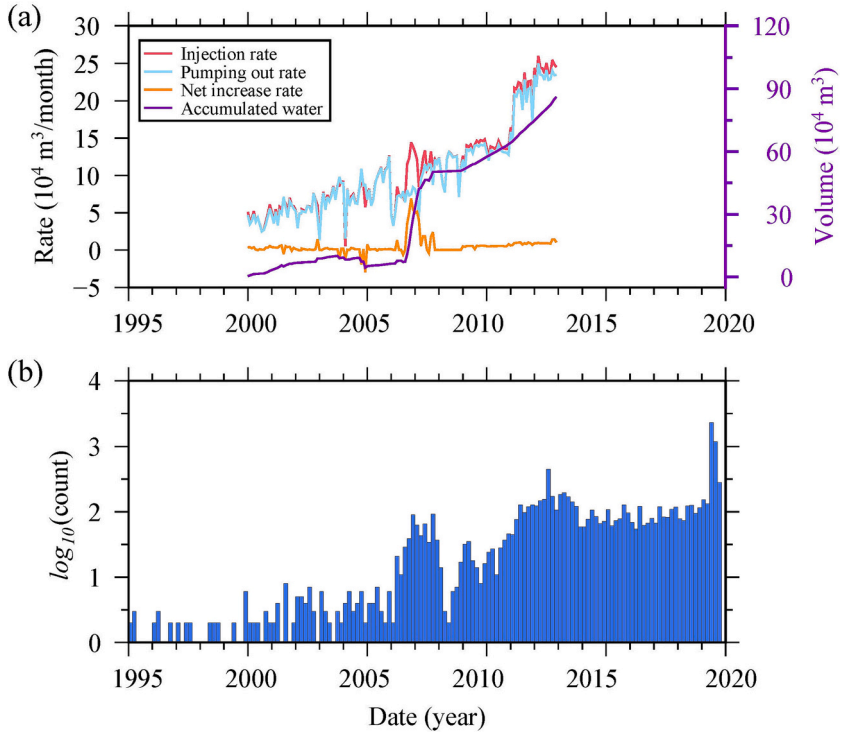

Fig. 3. (a) Water injection records of the Changning salt mine (Sun et al., 2017). The four curves are the water injection rate, pumping out rate, subsurface water increase rate, and subsurface accumulated water volume, respectively. The left vertical coordinate is for change rate and the right coordinate is for accumulated volume. (b) The regional seismicity in the Changning area. Note, the vertical axis is the logarithmic number of earthquakes per two-months.

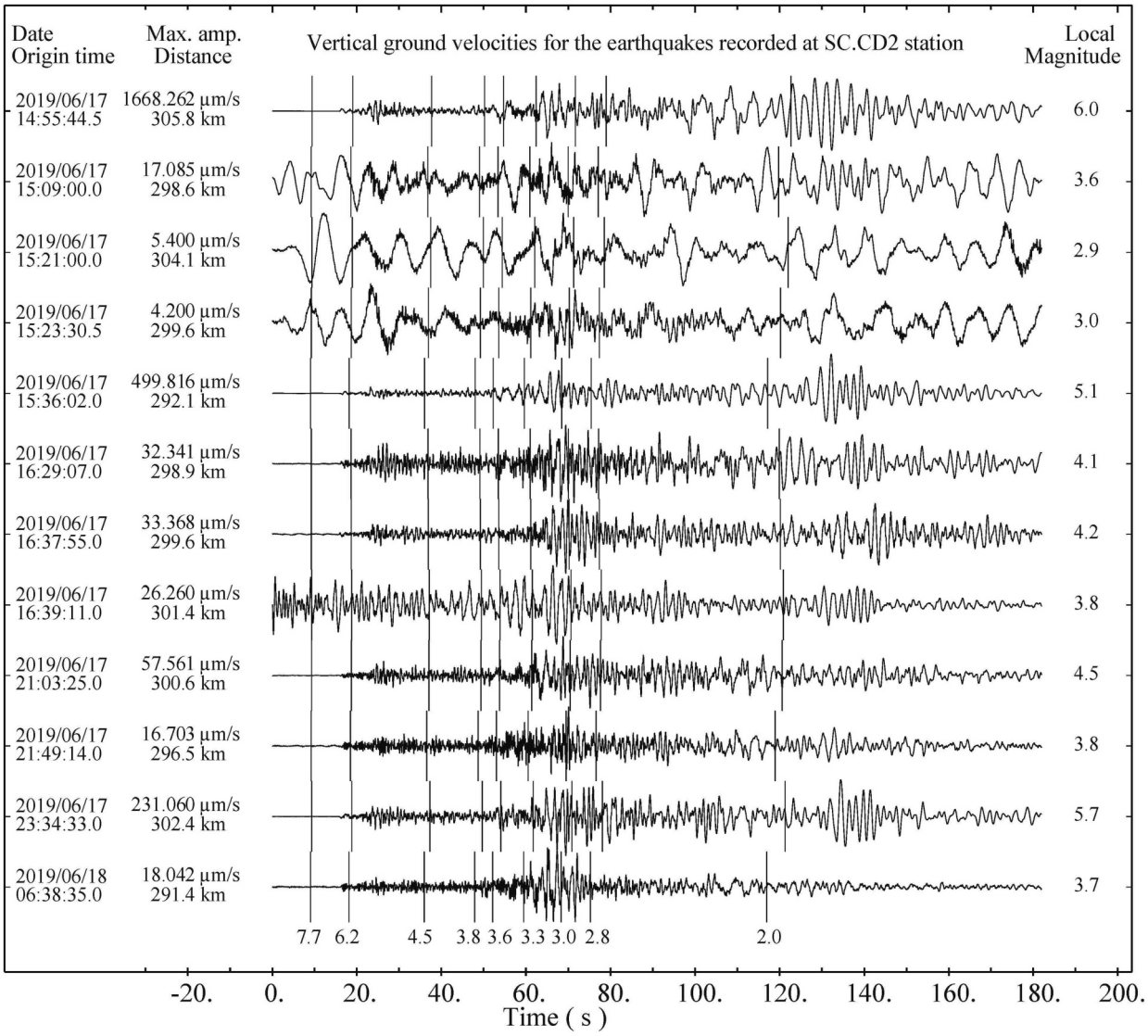

Fig. 4. Normalized vertical-component velocity seismograms bandpass filtered between 0.05 and 10.0 Hz for the mainshock (top trace) and selected aftershocks recorded by station SC.CD2, located in Sichuan Basin. Their dates, origin times, maximum velocities, and epicenter distances are listed on the left side, and their local magnitudes are labeled on the right side. The apparent group velocities are labeled by vertical bars.

seismograms (Kennett, 1986; Press and Ewing, 1952). It is sensitive to crust structures and relatively insensitive to the source radiation (e.g., Furumura and Kennett, 1997). It has also been used for magnitude measurements and nuclear discrimination studies, due to its stable propagation in the continental crust (e.g., Nuttli, 1986; Xie, 2005). In other words, once a regional Lg-wave attenuation model was established, we can directly remove the propagation effects and hence reasonably estimate source spectra for earthquakes (e.g., Shen et al., 2023; Zhao et al., 2013a; Zhao et al., 2010). Therefore, we retrieve the Lg-wave source excitation spectra for the 2019 June 17 Changning earthquake and its aftershocks at frequencies between 0.05 and 10.0 Hz based on a high-resolution broadband Lg-wave attenuation model developed by Zhao et al. (2013a). Then, we invert their seismic moments and corner frequencies and estimate the variations of stress drops for the entire 2019 Changning earthquake sequence. The possible relationship between injection activities and the Changning earthquake sequence is further investigated by checking the dependence of the stress drop on earthquake size, focal depth, and distance to the salt mining site.

2. Geological setting and industrial injection activities

Formed in the Tethys and Pacific tectonic domains, the Sichuan Basin has undergone long-term tectonic evolution since the Archean and has featured a stable sedimentary environment since the Paleozoic (e.g., Wang et al., 2014). It is mainly characterized by a crystalline basement and sedimentary cover with fold-thrust systems and detachment structures (e.g., Chen et al., 2014). The Sichuan Basin behaves as a rigid block with weak internal deformation (Wang et al., 2001). The study area in this paper features a complex anticline and syncline structure (Fig. 1a) with a well-developed underground microfracture system, which is caused by multiple deformations, including Caledonian, Hercynian, Indosinian, Yanshanian, and Himalayan tectonic movements (e.g., Long et al., 2020; Ruan et al., 2008). The upper crust of the Shuanghe area shows highly variable anisotropy reflecting a combined effect of complex local structure and stress field (Yang et al., 2022). The Changning anticline is a large basement fault-bend fold asymmetric anticline and contains numerous high-angle thrusts with dominant strikes between 304° and 348° (He et al., 2019; Sun et al., 2017; Wang et al., 2013).

The interior and surrounding areas of the Sichuan Basin are rich in salt deposits, petroleum, and gas resources (He et al., 2019). The

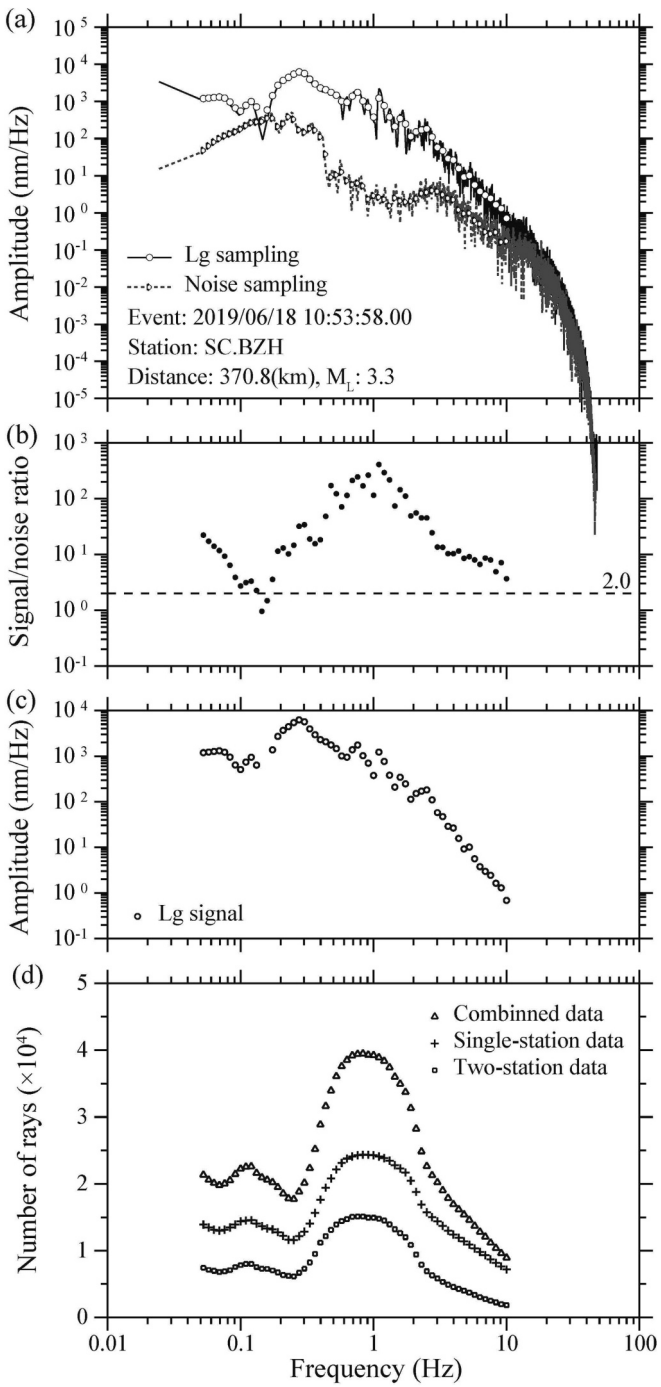

Fig. 5. Sample of the Lg-wave data processing. (a) The raw Lg-wave spectra (circles) from the mainshock recorded at station SC.BZH and the corresponding noise spectra (triangles), (b) signal-to-noise ratios (SNR), (c) noise corrected Lg-wave spectra, and (d) the numbers of available rays at individual frequencies. The dashed line in (b) illustrates the threshold of 2.0 to exclude low-quality data.

exploitation of salt mines has lasted for about a century and shale gas has been exploited for over ten years. The injection of a large amount of fluid has continuously affected the Changning area and had the potential risk to induce earthquakes (Lei et al., 2019b; Liu and Zahradník, 2020) (Fig. 1a). Several gas reservoirs are well developed in the lower Longmaxi Formation in the Changning shale gas block in Shangluo in the southern part of our study area (e.g., Chen et al., 2014). For shale gas prospecting, vertical wells were drilled in 2008 and horizontal wells were exploited in 2011 (Lei et al., 2017). The seismicity has increased dramatically since shale gas hydraulic fracturing began in the horizontal wells in 2014. In the Shuanghe area, several wells were drilled 30 years ago for salt production, and these wells extended down to the upper Sinian Dengying Formation at depths ranging from 2.7 to 3.0 km (e.g., Ruan et al., 2008). During salt production, freshwater was injected into the salt layer to dissolve the salt, and the brine was then pumped out. However, a larger amount of water injected into the subsurface cannot be completely pumped out and was left in the subsurface. The net increase of the subsurface water, i.e., the difference between the injected and pumped out volumes, correlates well with seismicity in the Shuanghe salt mine (Ruan et al., 2008), as illustrated in Fig. 3. Since 1990, high-pressure water has been injected using the conventional single-well technology, i.e., injection and pumping at the same well, and the volume of water loss exhibits a good correlation with enhanced seismicity in this area. After 2004, salt mining was performed using differentiated injection and pumping wells connected by subterranean horizontal wells (Fig. 1b), which further increased seismic activities in the Shuanghe area (e.g., Sun et al., 2017). Even though injection and pumping data are not available after 2013, the seismicity in this area remains high, notably including the 2019 Changning earthquake, indicating that the injected volume is still increasing.

3. Data and methods

3.1. Regional data set

The 2019 June 17 Changning earthquake and its aftershocks were well recorded by the China Earthquake Network Center (CENC) (Zheng et al., 2009). According to the CENC catalog, 94 aftershocks with local magnitudes higher than 2.8 occurred before 2019 September 30. We obtained the locations and origin times of the mainshock and its aftershocks from the CENC catalog and collected their seismograms recorded at 597 CENC stations from the China National Digital Seismic Network (Fig. 2). All stations are equipped with broadband instruments that have a sampling rate of 100 per second. Most of these seismograms are characterized by weak P-waves, strong Lg-waves, poorly developed S-waves, and well-developed short-period Rayleigh waves, reflecting the typical features of shallow-source earthquakes and propagation through shallow low-velocity sedimentary layers (Fig. 4).

3.2. Lg-wave amplitude spectrum

Compared with direct body waves, the Lg-wave is less sensitive to source radiation patterns and often serves as a robust tool to measure source spectra (e.g., Fan and Lay, 2002). The Lg wave signals were sampled using a group velocity window between 3.6 and 3.0 km/s (refer to Figs. 4 and 5) from the vertical component broadband regional waveform data. The window length is $\Delta/18\,sec.$, where Δ is the epicentral distance in km. Therefore, the window length is epicentral distance dependent. A time window of the same length was applied before the first P-wave arrival to sample the pre-event noise series. Next, the Fourier transform is used to calculate the spectra for both Lg-waves and the noise series. These spectra are sampled at 58 individual frequencies log-evenly distributed between 0.05 and 10.0 Hz according to the following equation (Zhao et al., 2010)

$$A(f) = \sqrt{\frac{1}{M-1}\sum_{i=1}^{M}[A(f_i)]^2}, \tag{1}$$

where $A(f)$ is the spectral amplitude at the nominal frequency f; $A(f_i)$ is the Fourier spectral amplitude; $f_i \in [f_1, f_2]$, f_1, and f_2 can be calculated by $log_{10}f - log_{10}f_1 = log_{10}f_2 - log_{10}f = 0.02$; and M is the number of samples between f_1 and f_2. Then, we calculate the signal-to-noise ratio (SNR) and set it to 2.0 to discard low-quality data. Based on 3 assumptions: (1)

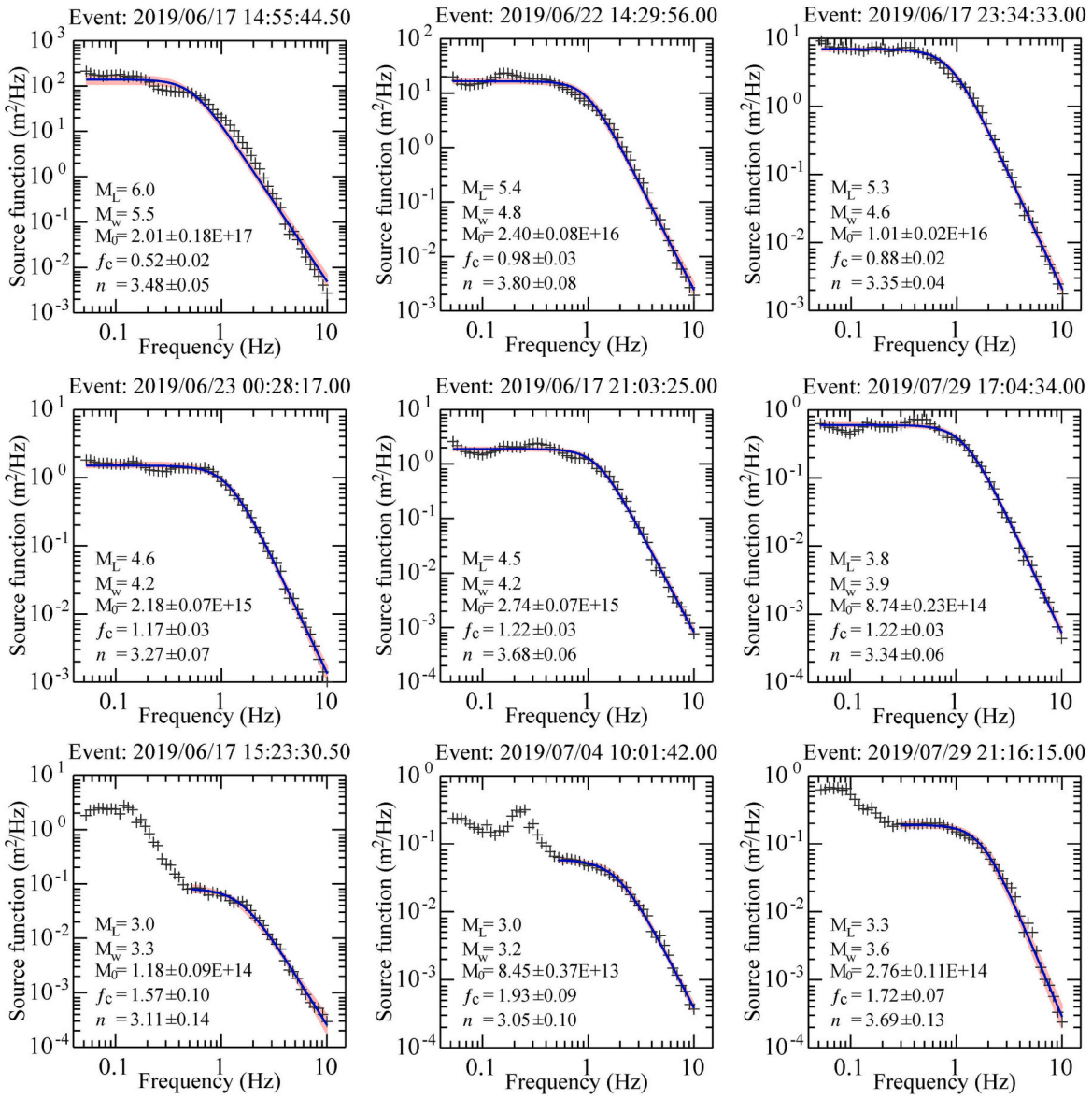

Fig. 6. Lg-wave source excitation spectra for selected events from the Changning earthquake sequence. The origin time of each event is on the top of each panel. The black crosses are source spectra inverted from the observed Lg-wave spectra. Solid lines are the best-fit source models with variable high-frequency falloff rate n, and pink shades are their standard deviations. All the fitting frequency band widths for smaller earthquakes (M_L<3.5) are visually checked. The local magnitude M_L, moment magnitude M_w, seismic moment M_0, corner frequency f_c, and high-frequency falloff rate n along with their standard deviations, are labeled in each panel. (For interpretation of the references to colour in this figure legend, the reader is referred to the web version of this article.)

the seismic record is a superposition of signal and noise, (2) the noise is stationary over a certain period, and (3) the noise is uncorrelated with the signal (Ringdal et al., 1992; Schlittenhardt, 2001), we remove the noise from the observed spectra and using

$$A_S^2(f) = A_O^2(f) - A_N^2(f), \tag{2}$$

to obtain the Lg-wave spectral amplitudes, where the subscripts S, O, and N denote the spectral amplitudes of the true signal, observed waveform, and noise, respectively.

3.3. Source spectral function

At a given frequency, the Lg-wave amplitude A_{kj} of event k recorded by station j can be expressed as

$$A_{kj} = S_k G_{kj} \Gamma_{kj} P_j r_{kj}, \tag{3}$$

where S_k is the source term, G_{kj} is the geometrical spreading factor and can be written as $G_{kj} = \left(\Delta_0 \Delta_{kj}\right)^{-1/2}$, where Δ_{kj} is the distance between event k and station j, and Δ_0 is the reference distance fixed at 100 km (Street et al., 1975); P_j is the site response; and r_{kj} is the accumulated random effects during Lg-wave propagation. Γ_{kj} is the attenuation along the path from event k to station j and can be calculated based on an established high-resolution broadband Lg-wave Q model (Fig. 2, Zhao et al., 2013a). With the known crustal attenuation model and geometric spreading term, the propagation effects from the source to a station can be directly removed. We employ a joint inversion to solve the source term and site response based on both the single- and two-station Lg-wave amplitude (Zhao and Mousavi, 2018; Zhao et al., 2013a; Zhao et al., 2013b)

$$\begin{bmatrix} \boldsymbol{H}_s \\ \boldsymbol{H}_t \end{bmatrix} = \begin{bmatrix} \boldsymbol{A}_s \\ \boldsymbol{A}_t \end{bmatrix} \bullet \delta\mathbf{Q} + \begin{bmatrix} \boldsymbol{E} \\ \mathbf{0} \end{bmatrix} \bullet \delta\mathbf{S} + \begin{bmatrix} \boldsymbol{F}_s \\ \boldsymbol{F}_t \end{bmatrix} \bullet \delta\mathbf{P}, \tag{4}$$

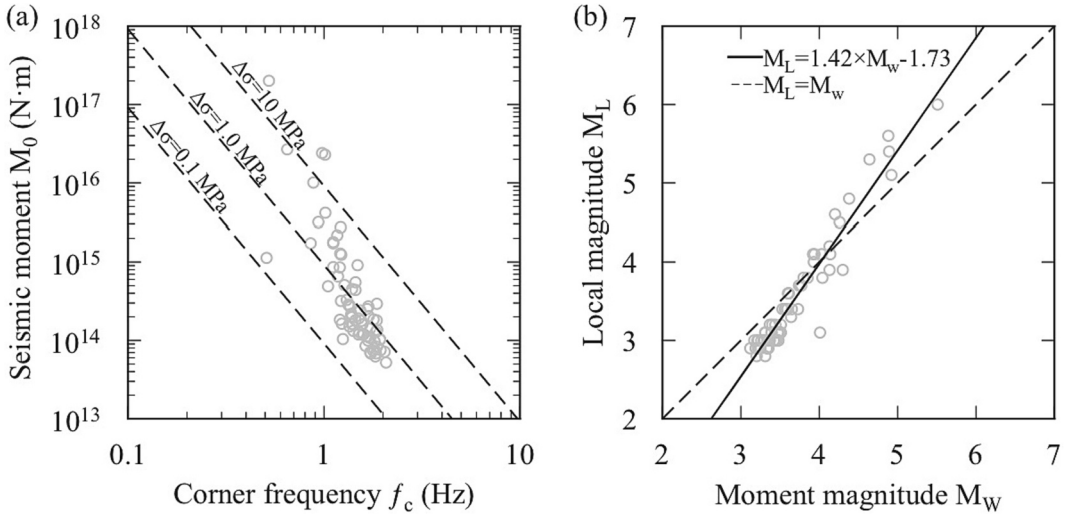

Fig. 7. (a) Seismic moment M_0 (N·m) versus corner frequency f_c (Hz) for 95 earthquakes in this study. The dashed lines mark constant stress drops for 0.1, 1, and 10 MPa. (b) M_L measured by CENC versus M_w derived from the seismic moment M_0. The solid line represents the best fit relation and the dashed line represents the unit relation $M_L = M_w$.

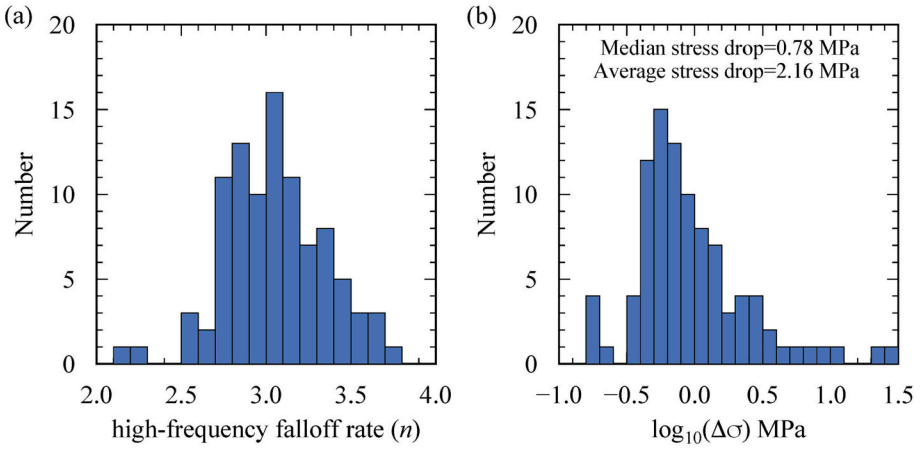

Fig. 8. Histograms illustrating the distributions of (a) the high-frequency falloff rates and (b) logarithmic stress drops.

where matrices **A**, **E**, and **F** link the Lg spectra residuals with the attenuation perturbations δ**Q**, source perturbations δ**S**, and perturbations in site responses δ**P**, respectively, and the random error term is neglected. The subscripts *s* and *t* indicate factors either relating to the single- or two- station data. $\boldsymbol{H}_s$ and $\boldsymbol{H}_t$ are vectors composed of residuals between the observed and synthetic Lg spectra. Illustrated in Fig. 5d are the numbers of available single-station, two-station, and total data points versus the frequency. Due to the variations in signal amplitude, noise level, and attenuation, these numbers vary with frequencies. Taking the advantage of the high-quality Lg-wave dataset, we obtained a broadband high-resolution crustal attenuation model for the Sichuan Basin and its surrounding areas (He et al., 2021; Zhao et al., 2013a), which enable us to separate the attenuation term directly. Although the regional broadband Lg wave Q model is used to remove the attenuation effect in the data, a huge amount of amplitude data used in this study allow us to further refine this process. An unknown factor δ**Q** is inserted in the inversion. We allow it to take up to 10% variation above the regional Q model to accommodate the effect of local attenuation fluctuations. The perturbations in site responses δ**P** were constrained by $\sum \delta P = 0$ and $\sum|\delta P| < \varepsilon$, where ε is an empirical value for normalizing the site responses (Fig. S1 and S2) (e.g., Ottemöller et al., 2002; Zhao and Mousavi, 2018). By using the LSQR algorithm (Least Square QR factorization, Paige and Saunders, 1982), we solve Eq. (4) for retrieving the source spectra for the selected 95 events in the Changning earthquake sequence.

To obtain the scalar seismic moment M_0 and corner frequency f_c, we use a general source model

$$S(f) = \frac{M_0}{4\pi\rho\nu^3[1 + (f/f_c)^n]} \tag{5}$$

to fit the observed Lg spectra, where ρ and ν are the density and shear wave velocity in the source area, and n is the high-frequency falloff rate (Abercrombie, 1995; Boatwright, 1980). We assume $\rho = 2.7$ g/cm^3 and $\nu = 3.5$ km/s for the Sichuan Basin (Bao et al., 2015). Eq. (5) with $n = 2$ gives the commonly used ω^{-2} source model (Brune, 1970). Because the high-frequency falloff rate can be associated with the heterogeneity of rupturing process and near-source effects, it usually varies between approximately 1.5 and 4.0 (Abercrombie, 1995; Boatwright, 1980; Dahlen, 1974; Madariaga, 1976; Prieto et al., 2004). Therefore, we allow the n to vary along with seismic moment M_0 and corner frequency f_c to solve for the best fitting source parameters.

For the Changning earthquake sequence, the observed Lg-wave spectra are often affected by low-frequency noises (Fig. 5a), which are resulted from ambient noise, coda waves of preceding phases, low-

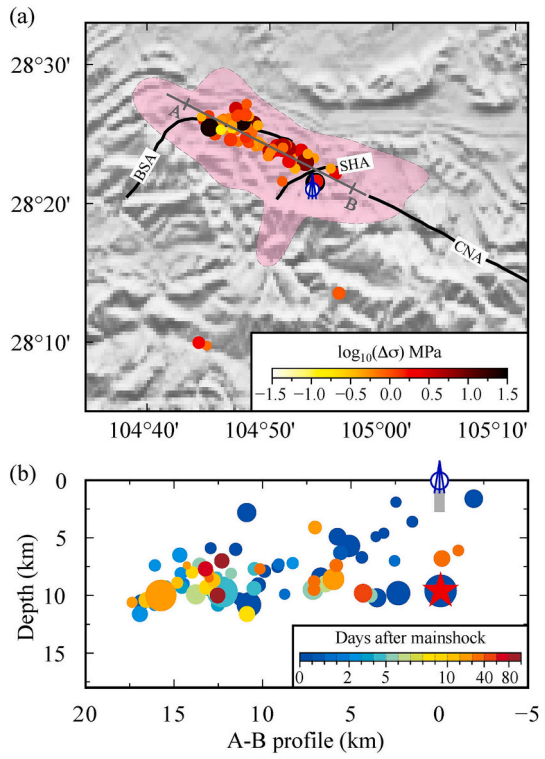

Fig. 9. The stress drops of the 2019 June 17 Changning earthquake sequence, (a) in map view and (b) along profile A-B. The location of the profile A-B is shown as the gray line in (a), corresponding to the major axis of the aftershock zone. The pink area in (a) represents the Shuanghe salt mining area (Lei et al., 2019b), and is overlayed on the grayscale topography. The drilling symbol represents the location of the water injection area. The size of the circle is proportional to the stress drop value. The colors of circles in (b) indicate the time after the mainshock (in days). The gray rectangular under the drilling symbol represents the depth of the water injection well (2.5– 2.9 km). Note the tendency that events with larger stress drops are close to the edge of the fracture. (For interpretation of the references to colour in this figure legend, the reader is referred to the web version of this article.)

frequency surface waves, or even coda-waves from previous earthquakes in the sequence. Traditionally, two approaches were often used to eliminate these noisy data, setting a proper SNR threshold to reject the noisy data (e.g., Abercrombie, 2014; Boyd et al., 2017; Drouet et al., 2005), or setting a truncation frequency to directly drop the low-frequency part of the spectrum (e.g., Abercrombie, 1995; Allmann and Shearer, 2007; Ottemöller and Havskov, 2003). The SNR is calculated from noise amplitude, mostly the pre-event noise and sometimes the pre-phase noise. Owing to the complex noise sources mentioned above, the low-frequency noises are not necessarily reflected in the pre-event noise. For example, the contamination from the surface wave usually enters the Lg wave from the latter section of the Lg window. This makes the SNR based on the pre-event noise or pre-phase noise not an effective index to judge these low-frequency data. Spectra from larger earthquakes tend to have high absolute amplitudes and abundant low-frequency contents, thus less affected by the low-frequency noise. On the contrary, smaller earthquakes have low absolute amplitudes and abundant high-frequency contents. Their low-frequency spectra can easily fall into the low-frequency noise. On the other hand, small events tend to have relatively higher corner frequencies. The extremely low-frequency spectral contents are not necessary to determine the seismic moment and corner frequency. Therefore, we combine both methods in data processing. We first use an SNR threshold of 2.0 to obtain source spectra on the whole frequency band between 0.05 and 10.0 Hz. Then, we check all Lg-wave source spectra to determine the truncation frequencies for all events. The large and obvious step-like shapes can be generally found in the earthquakes with magnitudes lower than 3.5. For large events with $M_L \geq 3.5$, we keep the entire spectra. For small events with $M_L < 3.5$, we visually check their spectra and set a truncation frequency to eliminate their very low frequency section. When visually choosing the truncation frequency, we try to drop the large step-shaped low-frequency contents and ensure enough flat parts to precisely evaluate source parameters. The simulated annealing (Kirkpatrick et al., 1983), a nonexhaustive global optimization algorithm, is used to estimate the M_0, f_c, and n by minimizing the L2 norm of differences between observed and synthetic Lg source spectra. The bootstrap method (Efron, 1983) is further used to estimate the errors for the M_0, f_c, and n. We also test different thresholds of SNR > 3.0, 4.0, 5.0, and 10.0 and find the results are relatively stable (Fig. S3). Finally, a threshold SNR > 2.0 is adopted in our calculation.

The moment magnitude M_w can be estimated from the inverted scalar moment M_0 using the formula proposed by Hanks and Kanamori (1979).

$$M_w = \frac{2}{3} logM_0 - 6.03, \tag{6}$$

From this, the scaling relation between the M_L and M_w can be obtained.

3.4. Stress drop

Based on the circular fault model, the stress drop can be calculated as (e.g., Allmann and Shearer, 2009; Eshelby, 1957)

$$\Delta\sigma = \frac{7M_0}{16}\left(\frac{1}{r}\right)^3 \tag{7}$$

where r is the radius of the circular fault and can be expressed as

$$r = \frac{kv}{f_c} \tag{8}$$

where k is a constant depending on the specific theoretical source model. If the rupture velocity is assumed to be $0.9v$, k is 0.21 for a S-wave source (Madariaga, 1976). However, currently the theoretical model for Lg-wave source is unavailable. From eqs. (7) and (8), the k value only slightly influences the absolute value of the stress drop, while does not change the relative variations of stress drops in a seismic sequence (e.g., Kaneko and Shearer, 2014). Therefore, we adopt the k value for the S-wave source to calculate the Lg-wave stress drop. Finally, the stress drop can be calculated based on the previously determined M_0 and f_c as follows,

$$\Delta\sigma = \frac{7M_0}{16}\left(\frac{f_c}{0.21v}\right)^3 \tag{9}$$

4. Results

Using the above-mentioned method, we obtained the Lg-wave source spectra and calculated the seismic moments, corner frequencies, and stress drops for the 2019 Changning earthquake and its aftershock sequence (Table S1). The source spectra were inverted independently at individual frequencies without using any a priori constraint between frequencies. The source model Eq. (5) is used to fit the observed source spectra in a selected frequency band (Fig. 6). The seismic moment, corner frequency, and high-frequency falloff rate were estimated to be 2.01×10^{17} N • m, 0.52 Hz, and 3.48, respectively, for the mainshock. Fig. 7a plots the seismic moment versus corner frequency. The results show that seismic moments range from 10^{14} to 10^{17} N·m and the corner frequencies are between 0.5– 2.1 Hz. Fig. 7b shows the moment magnitude M_w calculated using eq. (6) versus local magnitude M_L from CENC for the 2019 Changning earthquake sequence. A magnitude scaling can be obtained between M_w and M_L by using linear regression,

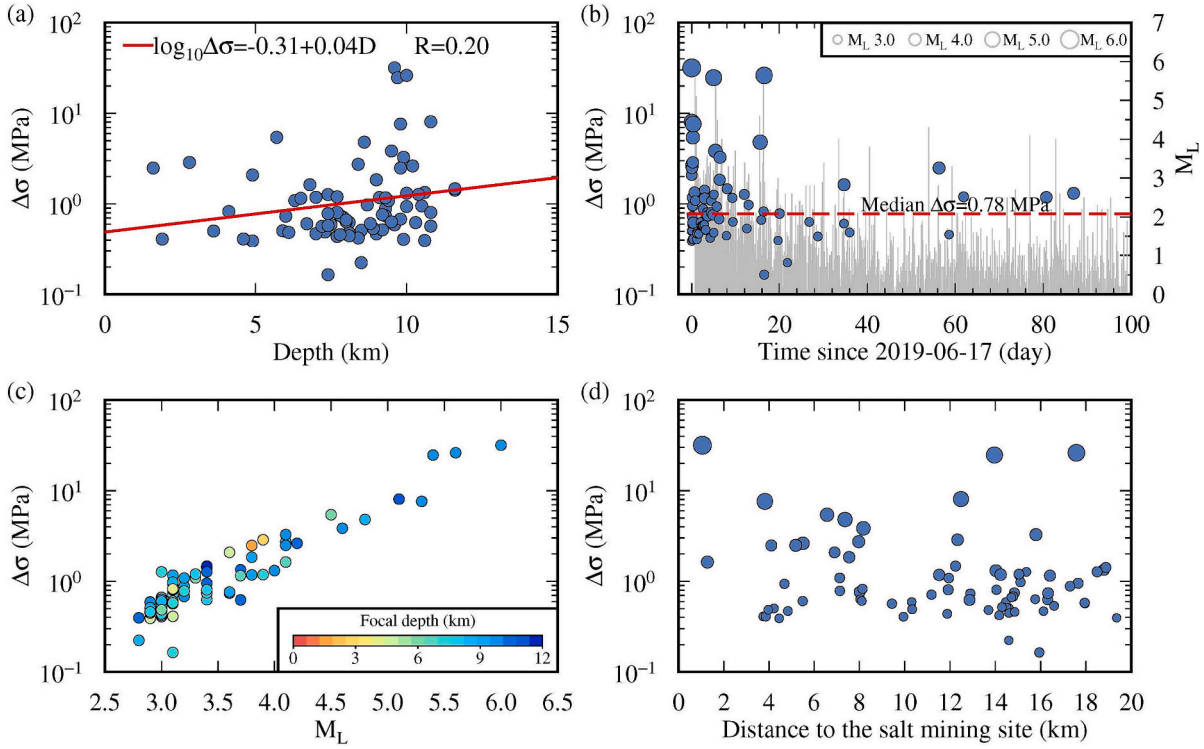

Fig. 10. Stress drops from the 2019 June 17 Changning earthquake sequence versus other variables. (a) Stress drops (in MPa) versus focal depths, where the red line represents linear regression with a correlation coefficient of 0.20. (b) Stress drops versus elapsed time since the mainshock. The horizontal dashed line marks the median stress drop of aftershocks, and the vertical gray lines represent the seismicity with their heights denoting the magnitudes. (c) Stress drops versus local magnitudes, with their focal depths, are colour-coded. (d) Stress drop versus distance away from the injection well in the salt mining area. Note that the distance between the earthquake and the salt mining site refers to the two-dimensional distance on the map. (For interpretation of the references to colour in this figure legend, the reader is referred to the web version of this article.)

$$M_L = 1.42M_w - 1.73 \quad (10)$$

Some non-linear relationships for M_W-M_L scaling were also proposed in other areas (e.g., Goertz-Allmann et al., 2011a; Munafò et al., 2016). For example, Bethmann et al. (2011) suggested that for magnitudes ranging between 3.0 and 5.0, M_w and M_L may be equivalent, whereas for smaller earthquakes the scaling changes to $M_L \sim 1.5\,M_w$. The difference between M_w and M_L may be because the two scales sample different frequency bands of the source spectra. This can be further affected by frequency-dependent attenuation and scattering along the propagation path (e.g., Munafò et al., 2016).

Figure 8 illustrates distributions of both high-frequency falloff rates and logarithmic stress drops. The inverted high-frequency falloff rates are mainly distributed between 2.0 and 4.0 (Fig. 8a). By using a variable n, the source spectra can be better fitted and both the M_0 and f_c can be reasonably determined. Therefore, the stress drops can be reliably obtained within a relatively large range between 0.1 and 32 MPa, with the median and average values of 0.78 MPa and 2.16 MPa, respectively (Fig. 8b).

The earthquakes are mostly concentrated in the Shuanghe area (Fig. 9a), implying a close relationship with water injection activities. The mainshock is fairly close (~1 km) to the Changning salt mine, where a large amount of water has been injected to a depth of approximately 3 km for over 20 years (Lei et al., 2019b). To investigate the spatial variation of stress drops along the Shuanghe anticline, we project all earthquakes to a cross-section with a strike of 300°. Over a distance of about 20 km, stress drops show large variations, which may reflect spatially varying fault strength and heterogeneous stress distribution (Fig. 9b). Two aftershocks at the edge of the coseismic rupture area feature stress drop values close to that of the mainshock, which may be due to the stress perturbations related to the rupture of the mainshock (e.g., Das and Henry, 2003; Gu et al., 1982). A roughly log-linear increase in stress drop with focal depth was examined in Fig. 10a, though the results are relatively scattered. As seen in Fig. 10a and b, almost all aftershocks with stress drops larger than 3 MPa have their magnitudes larger than 4.5 and focal depths deeper than 8 km. These events probably fall in the low-permeability basement layer and are not affected by the fluid injection. Thus, high normal stress is dominated. However, shallow aftershocks are mostly characterized by lower stress drops, and likely related to the long-term water injection, which lowers the normal stress of the fault surface (e.g., Ellsworth, 2013; Lengline et al., 2014).

Generally, the stress drops of an aftershock sequence change through time due to the accumulated local stress being released and the healing of the slip plane (e.g., Hauksson, 2014). For the 2019 Changning earthquake sequence, the M_L 5.4 and 5.6 aftershocks occurred 5 and 17 days after the mainshock, both with stress drops of about 25 MPa, comparable with the mainshock (32 MPa). In addition, the stress drops of some aftershocks remain higher than the median value over 80 days after the mainshock. The temporal pattern of a slow decline in the stress drops of the Changning earthquake sequence (Fig. 10b) was in contrast with the rapid falloff of stress drop within a month for 2008 Wenchuan aftershocks (Hua et al., 2009), a typical tectonic earthquake sequence. The difference may be related to the long-term water injection and complicated distribution of underground microcracks in the Changning salt mine. As a consequence, a longer time may be needed to recover to the equilibrium status for an induced earthquake after the region experienced such a large earthquake.

5. Discussions

In the present study, the moment magnitude of the 2019 Changning mainshock determined from the Lg wave source spectrum was $M_W = 5.5$,

which is slightly lower than 5.69 (Lei et al., 2019b) and 5.79 (Yi et al., 2019) obtained using moment tensor inversion, and 5.86 from geodetic inversion (Yang et al., 2021). Certain differences existed among different methods and authors. The stress drop obtained by us is 32 MPa based on the seismic moment and corner frequency, which is significantly higher than the 0.58–1.79 MPa obtained by Li et al. (2020) based on a relatively large rectangular fault model of 9–16 km long by 4–7 km wide. Generally, the selection of calculation method, source model, and parameter may lead to a large deviation for the absolute level of stress drop (e.g., Kaneko and Shearer, 2014). Also, the dynamic stress drops in our study based on radiation of seismic energy reflect tectonic unloading, while the static stress drop based on fault parameters only denotes net shear stress decreasing along the fault slip (Brown et al., 2015; Li et al., 2020). This is likely the reason why Li et al. (2020) obtained a much lower stress drop for the 2019 Changning earthquake. Therefore, many investigators indicated that the stress drop on the fault plane might be highly heterogeneous with high stress drop patches existed and tend to be revealed by the spectral method (e.g., Allmann and Shearer, 2009; Shearer et al., 2006).

Stress drop data can shed light on the physics of earthquakes (Shearer et al., 2006). According to self-similar earthquake scaling, in which the physics of large and small earthquakes are assumed to be fundamentally similar, the stress drop should be constant over a wide range of earthquake sizes (Aki, 1967). This scaling relationship is supported by observations showing that the median stress drop of global moderate to large earthquakes is approximately 4 MPa and does not vary with the seismic moment (Allmann and Shearer, 2009). However, for the 2019 Changning earthquake sequence, smaller earthquakes (M_L<3.5) systematically have anomalously low stress drops (<1 MPa), relative to those of aftershocks with magnitude higher than 5.0. Our results revealed that the stress drops generally increase with local magnitudes (Fig. 10c), which contradicts to the self-similar earthquake scaling pattern. This result may reflect that the larger aftershocks required greater momentum to break through stronger fault patches and that the rupture behaviors of the Changning earthquake sequence were likely different from those of typical tectonic earthquakes (Boyd et al., 2017). Such deviation was also observed for induced earthquake sequences in Oklahoma (Wu et al., 2018).

Many studies investigated differences in source properties between the induced and tectonic earthquakes, but there remained many different opinions. Although both types of earthquakes are driven by the accumulated strain, when it exceeds a critical value a fault can withstand, an induced earthquake is triggered by the increasing pore pressure, which reduces the friction on an existing fault plane, thus weakening its strength (e.g., Shapiro et al., 2011). Several studies reported that the induced earthquakes often involved in lower stress drops (e.g., Boyd et al., 2017; Chen and Shearer, 2011; Goertz-Allmann et al., 2011b; Sumy et al., 2017), but others suggested similar stress drops for induced and tectonic earthquakes (e.g., Huang et al., 2017; Wang et al., 2020; Wu et al., 2018). In Basel geothermal site, Goertz-Allmann et al. (2011b) observed a trend that stress drops increased with the increasing distance from the injection point because the higher pore pressure near the injection point can reduce the effective normal stress. This was later supported by the physical modeling involving fluid diffusion (Goertz-Allmann and Wiemer, 2013).

We investigated stress drops of the 2019 Changning earthquake sequence, including their spatial and temporary distributions, decay rate, and their variations versus the distance to the injection location. The results showed that the stress drops of the Changning earthquake sequence were highly complicated. The decay trend of the stress drops versus the distance to the injection point was not found. The 2D numerical simulation (Lei et al., 2019b) on the pore fluid diffusion along the fault plane suggested that, after enough long time, the diffusion front can reach a far distance, leaving a high pore pressure platform (~8 MPa) behind, within which the pore pressure is basically unchanged. In the Changning salt mine area, continuous fluid injection has lasted for >3 decades and caused approximately 850,000 m^3 of accumulated underground water by the end of 2013 (Lei et al., 2019b; Sun et al., 2017). This may imply the entire aftershock zone has reached overpressure, and it can also explain why an apparent trend between the stress drop and the distance to the injection center was not found.

The stress drops of the Changning earthquake sequence showed large fluctuations both temporally and spatially. Several strong aftershocks have stress drops comparable to the mainshock, while small aftershocks have systematically low stress drops. Most of the aftershocks with higher magnitudes and stress drops share similar focal mechanisms with the mainshock. This indicates that the entire aftershock sequence is still controlled by the regional stress field and local tectonics, while the industrial water injection only triggered this process (e.g., Huang et al., 2017). During the salt mining injection, the fluid not only diffused into the pore space in the solid rock to change the pore pressure but directly dissolved the solid salt. This process may extensively reduce the strength of the fault system in the Shuanghe anticline by raising the pore pressure. Moreover, under the influence of fluid injection, complex local stress fields, and abundant symbiotic faults, the surrounding faults are easier to slip. Therefore, we speculate that the two earthquakes with higher stress drops in the northwestern part of the aftershock zone may be triggered by the stress disturbance due to the 2019 Changning earthquake (e.g., Yi et al., 2019). The potential impact of fluid injection in salt mining, along with the complex local structures, may explain the large fluctuations of stress drops along the aftershock zone, as well as during the aftershock sequence. Once a large earthquake disturbs the regional stress field, it takes a long time to recover to its equilibrium status.

Earthquakes induced by industry activity always raise serious social concerns (e.g., Ellsworth et al., 2019). One of the most important issues is, in a given area, the maximum magnitude induced earthquakes could reach. van der Elst et al. (2016) considered that the largest earthquake magnitude for induced earthquakes is connected with pre-existing tectonic conditions and fluid injection volume. The Sichuan Basin, characterized by ~10 km thick sedimentary layer and well-developed fault systems and micro-cracks, could magnify the impact of fluid injections. The large amount and high rate of injected fluid, together with the removal of salt, may create a weakened underground fault system, causing large-scale ruptures. Therefore, it is necessary to closely monitor the potential risk of induced earthquakes and reduce the disaster damage.

Although the local seismicity is generally correlated to the water injection, careful investigation shows that, as illustrated in Fig. 3a and b, the variations of net water increase rate and total accumulated subsurface water, are not exactly synchronized with the seismic activity. The rise of seismicity proceeded the change of water injection by a very short period of one to two months. If the water injection record is accurate, it raises a question as if the injection triggered the earthquake or the earthquake also created channels to enhance the water diffusion, or maybe they are mutually affected. More observations are required to address this phenomenon.

6. Conclusions

We investigated the Lg-wave source spectra of the 2019 June 17 Changning earthquake and its 94 aftershocks which were associated with the fluid injection activities from the nearby salt mining. By fitting the observed spectra with theoretical source models, we further inverted their seismic moments and corner frequencies, from which the stress drops were estimated for the entire earthquake sequence. The stress drops varied from the lowest value of 0.1 MPa for small aftershocks to 32 MPa for the mainshock, with a median stress drop of 0.78 MPa for aftershocks. Our study observed a log-linear increase in stress drops versus increasing depth but with certain scatters around the trendline. Relatively lower stress drops for most shallow events may result from lowered normal stress caused by long-term injection. The stress drops

showed no apparent relation to the distances from the water injection well. By combining the stress drops and previous studies, it is suggested the impact of water injection has expanded to cover at least the entire aftershock zone of the 2019 Changning earthquake sequence.

CRediT authorship contribution statement

Lin Shen: Conceptualization, Writing – review & editing, Methodology, Writing – original draft, Investigation. **Lian-Feng Zhao:** Data curation, Methodology, Software, Supervision, Project administration, Writing – review & editing, Conceptualization, Funding acquisition. **Xiao-Bi Xie:** Writing – review & editing, Methodology, Supervision, Software, Conceptualization. **Xi He:** Software, Formal analysis, Data curation, Writing – review & editing, Investigation, Methodology. **Wei-Min Wang:** Supervision, Formal analysis, Methodology. **Zhen-Xing Yao:** Methodology, Supervision, Project administration, Funding acquisition.

Declaration of Competing Interest

The authors declare that they have no known competing financial interests or personal relationships that could have appeared to influence the work reported in this paper.

Data availability

The waveforms used in this study were collected from the Data Management Centre of China National Seismic Network at Institute of Geophysics, China Earthquake Administration, 2007, doi:10.11998/-SeisDmc/SN, http://www.seisdmc.ac.cn (Zheng et al., 2009). Data of the water injection in Changning salt mining area was provided by Xiao-Long Sun at the National Institute of Natural Hazards (Fig. 3a). Some figures were made using Generic Mapping Tools (https://forum.generic-mapping-tools.org/). The single- and two-station Lg amplitude data used in this study can be accessed at the World Data Centre for Geophysics, Beijing (https://doi.org/10.12197/2022GA005). The relocation result of the 2019 Changning earthquake sequence was provided by Xinglin Lei at the Geological Survey of Japan, The National Institute of Advanced Industrial Science and Technology (AIST), Japan (Lei et al., 2019b).

Acknowledgments

We thank Editor Gregory Houseman and an anonymous reviewer for their valuable comments that greatly improved the manuscript. This research is supported by the National Natural Science Foundation of China (U2139206, 41974054, 41974061, 42104055) and the China Seismic Experimental Site (2019CSES0103).

Appendix A. Supplementary data

Supplementary data to this article can be found online at https://doi.org/10.1016/j.tecto.2023.230139.

References

Abercrombie, R.E., 1995. Earthquake source scaling relationships from −1 to 5 M(L) using seismograms recorded at 2.5-km depth. J. Geophys. Res. 100, 24015–24036. https://doi.org/10.1029/95jb02397.

Abercrombie, R.E., 2014. Stress drops of repeating earthquakes on the San Andreas Fault at Parkfield. Geophys. Res. Lett. 41, 8784–8791. https://doi.org/10.1002/2014gl062079.

Aki, K., 1967. Scaling law of seismic spectrum. J. Geophys. Res. 72, 1217–1231. https://doi.org/10.1029/jz072i004p01217.

Allmann, B.P., Shearer, P.M., 2007. Spatial and temporal stress drop variations in small earthquakes near Parkfield, California. J. Geophys. Res. 112, B04305. https://doi.org/10.1029/2006jb004395.

Allmann, B.P., Shearer, P.M., 2009. Global variations of stress drop for moderate to large earthquakes. J. Geophys. Res. 114, B01310. https://doi.org/10.1029/2008JB005821.

Bao, X.W., Song, X.D., Li, J.T., 2015. High-resolution lithospheric structure beneath mainland China from ambient noise and earthquake surface-wave tomography. Earth Planet. Sci. Lett. 417, 132–141. https://doi.org/10.1016/j.epsl.2015.02.024.

Bethmann, F., Deichmann, N., Mai, P.M., 2011. Scaling relations of local magnitude versus moment magnitude for sequences of similar earthquakes in Switzerland. Bull. Seismol. Soc. Am. 101, 515–534. https://doi.org/10.1785/0120100179.

Boatwright, J., 1980. A spectral theory for circular seismic sources; simple estimates of source dimension, dynamic stress drop, and radiated seismic energy. Bull. Seismol. Soc. Am. 70, 1–27.

Boyd, O.S., McNamara, D.E., Hartzell, S., Choy, G., 2017. Influence of lithostatic stress on earthquake stress drops in North America. Bull. Seismol. Soc. Am. 107, 856–868. https://doi.org/10.1785/0120160219.

Brown, L., Wang, K., Sun, T., 2015. Static stress drop in the M-w 9 Tohoku-oki earthquake: Heterogeneous distribution and low average value. Geophys. Res. Lett. 42, 10595–10600. https://doi.org/10.1002/2015gl066361.

Brune, J.N., 1970. Tectonic stress and the spectra of seismic shear waves from earthquakes. J. Geophys. Res. 75, 4997–5009. https://doi.org/10.1029/JB075i026p04997.

Chen, S., Zhu, Y., Qin, Y., Wang, H., Liu, H., Fang, J., 2014. Reservoir evaluation of the lower Silurian Longmaxi formation shale gas in the southern Sichuan basin of China. Mar. Pet. Geol. 57, 619–630. https://doi.org/10.1016/j.marpetgeo.2014.07.008.

Chen, X., Shearer, P.M., 2011. Comprehensive analysis of earthquake source spectra and swarms in the Salton Trough, California. J. Geophys. Res. 116, B09309. https://doi.org/10.1029/2011jb008263.

Clerc, F., Harrington, R.M., Liu, Y., Gu, Y.J., 2016. Stress drop estimates and hypocenter relocations of induced seismicity near Crooked Lake, Alberta. Geophys. Res. Lett. 43, 6942–6951. https://doi.org/10.1002/2016gl069800.

Dahlen, F.A., 1974. On the ratio of P-wave to S-wave corner frequencies for shallow earthquake sources. Bull. Seismol. Soc. Am. 64, 1159–1180.

Das, S., Henry, C., 2003. Spatial relation between main earthquake slip and its aftershock distribution. Rev. Geophys. 41 https://doi.org/10.1029/2002rg000119.

Drouet, S., Souriau, A., Cotton, F., 2005. Attenuation, seismic moments, and site effects for weak-motion events: application to the Pyrenees. Bull. Seismol. Soc. Am. 95, 1731–1748.

Efron, B., 1983. Estimating the error rate of a prediction rule: Improvement on cross-validation. J. Am. Stat. Assoc. 78, 316–331. https://doi.org/10.2307/2288636.

Ellsworth, W.L., 2013. Injection-induced earthquakes. Science 341, 142. https://doi.org/10.1126/science.1225942.

Ellsworth, W.L., Giardini, D., Townend, J., Ge, S., Shimamoto, T., 2019. Triggering of the Pohang, Korea, earthquake (Mw 5.5) by Enhanced Geothermal System Stimulation. Seismol. Res. Lett. https://doi.org/10.1785/0220190102.

van der Elst, N.J., Page, M.T., Weiser, D.A., Goebel, T.H.W., Hosseini, S.M., 2016. Induced earthquake magnitudes are as large as (statistically) expected. J. Geophys. Res. 121, 4575–4590. https://doi.org/10.1002/2016jb012818.

Eshelby, J.D., 1957. The determination of the elastic field of an ellipsoidal inclusion, and related problems. Prec. Roy. Soc. London A241, 376–396.

Fan, G., Lay, T., 2002. Characteristics of Lg attenuation in the Tibetan Plateau. J. Geophys. Res. 107 (B10), 2256. https://doi.org/10.1029/2001JB000804.

Furumura, T., Kennett, B.L.N., 1997. On the nature of regional seismic phases—II. On the influence of structural barriers. Geophys. J. R. Astron. Soc. 129, 221–234.

Goertz-Allmann, B.P., Wiemer, S., 2013. Geomechanical modeling of induced seismicity source parameters and implications for seismic hazard assessment. Geophysics 78, KS25-KS39. https://doi.org/10.1190/geo2012-0102.1.

Goertz-Allmann, B.P., Edwards, B., Bethmann, F., Deichmann, N., Giardini, D., 2011a. A new empirical magnitude scaling relation for Switzerland. Bull. Seismol. Soc. Am. 101, 3088–3095.

Goertz-Allmann, B.P., Goertz, A., Wiemer, S., 2011b. Stress drop variations of induced earthquakes at the Basel geothermal site. Geophys. Res. Lett. 38, L09308. https://doi.org/10.1029/2011gl047498.

Gu, J.C., Xie, X.B., Zhao, L., 1982. On spatial distribution of large aftershocks of the sequence of a major earthquake and preliminary theoretical explanation. Acta Sismol. Sin. (In Chinese) 4 (4), 380–388.

Hanks, T.C., Kanamori, H., 1979. A moment magnitude scale. J. Geophys. Res. 84, 2348–2350. https://doi.org/10.1029/JB084iB05p02348.

Hauksson, E., 2014. Average stress drops of southern California earthquakes in the context of crustal geophysics: implications for fault zone healing. Pure Appl. Geophys. 172 (5), 1359–1370. https://doi.org/10.1007/s00024-014-0934-4.

He, D.F., Lu, R.Q., Huang, H.Y., Wang, X.S., Jiang, H., Zhang, W.K., 2019. Tectonic and geological setting of the earthquake hazards in the Changning shale gas development zone, Sichuan Basin, SW China. Pet. Explor. Dev. 46, 1051–1064. https://doi.org/10.1016/s1876-3804(19)60262-4.

He, X., Zhao, L.F., Xie, X.B., Shen, L., Wang, W.M., Yao, Z.X., 2020. Stress drop assessment of the August 8, 2017, Jiuzhaigou earthquake sequence and its tectonic implications. Earthq. Sci. 33, 1–16.

He, X., Zhao, L., Xie, X., Tian, X., Yao, Z., 2021. Weak crust in southeast Tibetan Plateau revealed by Lg-wave attenuation tomography: implications for crustal material escape. J. Geophys. Res. https://doi.org/10.1029/2020JB020748 e2020JB020748.

He, X., Zhao, L.-F., Xie, X.-B., Zhang, L., Yao, Z.-X., 2023. Eastward expansion of the Tibetan plateau: Insights from stress drops of the 2021 Ms 6.4 Yangbi, Yunnan and Ms 7.4 Maduo, Qinghai earthquake sequences in China. Front. Earth Sci. 11, 1081605. https://doi.org/10.3389/feart.2023.1081605.

Hough, S.E., 1997. Empirical green's function analysis: taking the next step. J. Geophys. Res. 102, 5369–5384. https://doi.org/10.1029/96jb03488.

Hua, W., Chen, Z.L., Zheng, S.H., 2009. A study on segmentation characteristics of aftershocks source parameters of Wenchuan M8.0 earthquake in 2008. Chin. J. Geophys. (in Chinese) 52 (2), 365–371. https://doi.org/10.1002/cjg2.1334.
Huang, Y., Ellsworth, W.L., Beroza, G.C., 2017. Stress drops of induced and tectonic earthquakes in the Central United States are indistinguishable. Sci. Adv. 3, e1700772 https://doi.org/10.1126/sciadv.1700772.
Kaneko, Y., Shearer, P.M., 2014. Seismic source spectra and estimated stress drop derived from cohesive-zone models of circular subshear rupture. Geophys. J. Int. 197, 1002–1015. https://doi.org/10.1093/gji/ggu030.
Kennett, B.L.N., 1986. Lg-waves and structural boundaries. Bull. Seismol. Soc. Am. 76, 1133–1141.
Kirkpatrick, S., Gelatt, C.D., Vecchi, M.P., 1983. Optimization by simulated annealing. Science 220, 671–680. https://doi.org/10.1126/science.220.4598.671.
Lei, X., Su, J., Wang, Z., 2020. Growing seismicity in the Sichuan Basin and its association with industrial activities. Sci. China Earth Sci. 63, 1633–1660. https://doi.org/10.1007/s11430-020-9646-x.
Lei, X.L., Huang, D.J., Su, J.R., Jiang, G.M., Wang, X.L., Wang, H., Guo, X., Fu, H., 2017. Fault reactivation and earthquakes with magnitudes of up to Mw4.7 induced by shale-gas hydraulic fracturing in Sichuan Basin, China. Sci. Rep. 7, 7971. https://doi.org/10.1038/s41598-017-08557-y.
Lei, X.L., Wang, Z.W., Su, J.R., 2019a. The December 2018 ML 5.7 and January 2019 ML 5.3 earthquakes in South Sichuan basin induced by shale gas hydraulic fracturing. Seismol. Res. Lett. 90 https://doi.org/10.1785/0220190182.
Lei, X.L., Wang, Z.W., Su, J.R., 2019b. Possible link between long-term and short-term water injections and earthquakes in salt mine and shale gas site in Changning,south Sichuan Basin, China. Earth Planet. Phys. 3 (6), 510–525. https://doi.org/10.26464/epp2019052.
Lengline, O., Lamourette, L., Vivin, L., Cuenot, N., Schmittbuhl, J., 2014. Fluid-induced earthquakes with variable stress drop. J. Geophys. Res. 119, 8900–8913. https://doi.org/10.1002/2014jb011282.
Li, W., Ni, S.D., Zang, C., Chu, R.S., 2020. Rupture directivity of the 2019 Mw 5.8 Changning, Sichuan, China, earthquake and implication for induced seismicity. Bull. Seismol. Soc. Am. https://doi.org/10.1785/0120200013.
Liu, J., Zahradník, J., 2020. The 2019 Mw 5.7 Changning earthquake, Sichuan Basin, China: a shallow doublet with different faulting styles. Geophys. Res. Lett. 47 https://doi.org/10.1029/2019GL085408.
Long, F., Zhang, Z.W., Qi, Y.P., Liang, M.J., Ruan, X., Wu, W.W., Jiang, G.M., Zhou, L.Q., 2020. Three dimensional velocity structure and accurate earthquake location in Changning–Gongxian area of southeast Sichuan. Earth Planet. Phys. 4, 1–15. https://doi.org/10.26464/epp2020022.
Madariaga, R., 1976. Dynamics of an expanding circular fault. Bull. Seismol. Soc. Am. 66, 639–666. https://doi.org/10.1007/BF02246368.
Munafò, I., Malagnini, L., Chiaraluce, L., 2016. On the relationship between Mw and ML for small earthquakes. Bull. Seismol. Soc. Am. 106, 2402–2408. https://doi.org/10.1785/0120160130.
Nuttli, O.W., 1973. Seismic wave attenuation and magnitude relations for eastern North America. J. Geophys. Res. 78, 876–885. https://doi.org/10.1029/JB078i005p00876.
Nuttli, O.W., 1986. Yield estimates of nevada test site explosions obtained from seismic Lg waves. J. Geophys. Res. 91, 2137–2151. https://doi.org/10.1029/JB091iB02p02137.
Oth, A., 2013. On the characteristics of earthquake stress release variations in Japan. Earth Planet. Sci. Lett. 377-378, 132–141. https://doi.org/10.1016/j.epsl.2013.06.037.
Ottemöller, L., Havskov, J., 2003. Moment magnitude determination for local and regional earthquakes based on source spectra. Bull. Seismol. Soc. Am. 93, 203–214.
Ottemöller, L., Shapiro, N.M., Singh, S.K., Pacheco, J.F., 2002. Lateral variation of Lg wave propagation in southern Mexico. J. Geophys. Res. 107 https://doi.org/10.1029/2001JB000206. ESE 3-1 - ESE 3-13.
Paige, C.C., Saunders, M.A., 1982. LSQR an algorithm for sparse linear-equations and sparse least-squares. ACM Trans. Math. Softw. 8, 43–71. https://doi.org/10.1145/355984.355989.
Press, F., Ewing, M., 1952. Two slow surface waves across North America. Bull. Seismol. Soc. Am. 42, 219–228.
Prieto, G.A., Shearer, P.M., Vernon, F.L., Kilb, D., 2004. Earthquake source scaling and self-similarity estimation from stacking P and S spectra. J. Geophys. Res. 109, B08310.
Qian, H., Tang, R.C., 1992. Seismo-geological features of the the Sichuan basin. Earthq. Res. Sichuan (in Chin.) 3, 13–18.
Ringdal, F., Marshall, P.D., Alewine, R.W., 1992. Seismic yield determination of soviet underground nuclear-explosions at the Shagan river test site. Geophys. J. Int. 109, 65–77. https://doi.org/10.1111/j.1365-246X.1992.tb00079.x.
Ruan, X., Cheng, W., Zhang, Y., Li, J., Chen, Y., 2008. Research of the activity of earthquakes induced by water injection of salt mining in Changning county, Sichuan province. Earthq. Res. China 24, 226–234.
Schlittenhardt, J., 2001. Teleseismic Lg of Semipalatinsk and Novaya Zemlya nuclear explosions recorded by the GRF (Grafenberg) array: comparison with regional Lg (BRV) and their potential for accurate yield estimation. Pure Appl. Geophys. 158, 2253–2274. https://doi.org/10.1007/Pl00001148.
Shapiro, S.A., Krüger, O.S., Dinske, C., Langenbruch, C., 2011. Magnitudes of induced earthquakes and geometric scales of fluid-stimulated rock volumes. Geophysics 76. https://doi.org/10.1190/GEO2010-0349.1. WC55–WC63.
Shearer, P.M., Prieto, G.A., Hauksson, E., 2006. Comprehensive analysis of earthquake source spectra in southern California. J. Geophys. Res. 111, B06303. https://doi.org/10.1029/2005jb003979.
Shen, L., Zhao, L.-F., Xie, X.-B., Yang, G., Yao, Z.-X., 2023. Extremely weak Lg attenuation reveals ancient continental relicts in the South China block. Earth Planet. Sci. Lett. 611, 118144 https://doi.org/10.1016/j.epsl.2023.118144.
Street, R.L., Herrmann, R.B., Nuttli, O.W., 1975. Spectral characteristics of the Lg wave generated by Central United States earthquakes. Geophys. J. Int. 41, 51–63. https://doi.org/10.1111/j.1365-246X.1975.tb05484.x.
Sumy, D.F., Neighbors, C.J., Cochran, E.S., Keranen, K.M., 2017. Low stress drops observed for aftershocks of the 2011Mw5.7 Prague, Oklahoma, earthquake. J. Geophys. Res. 122, 3813–3834. https://doi.org/10.1002/2016jb013153.
Sun, X.L., Yang, P.T., Zhang, Z.W., 2017. A study of earthquakes induced by water injection in the Changning salt mine area, SW China. J. Asian Earth Sci. 136, 102–109. https://doi.org/10.1016/j.jseaes.2017.01.030.
Wang, B., Harrington, R.M., Liu, Y., Kao, H., Yu, H., 2020. A study on the largest hydraulic-fracturing-induced earthquake in Canada: observations and static stress-drop estimation. Bull. Seismol. Soc. Am. 111, 1392–1404. https://doi.org/10.1785/0120190261.
Wang, E., Meng, K., Su, Z., Meng, Q., Chu, J.J., Chen, Z., Wang, G., Shi, X., Liang, X., 2014. Block rotation: Tectonic response of the Sichuan basin to the southeastward growth of the Tibetan Plateau along the Xianshuihe-Xiaojiang fault. Tectonics. 33, 686–718. https://doi.org/10.1002/2013tc003337.
Wang, Q., Zhang, P.Z., Freymueller, J.T., Bilham, R., Larson, K.M., Lai, X., You, X., Niu, Z., Wu, J., Li, Y., 2001. Present-day crustal deformation in China constrained by global positioning system measurements. Science 294, 574–577. https://doi.org/10.1126/science.1063647.
Wang, S.Z., Zhong Quan, L.I., Guo, M., Hong Kui, L.I., 2013. Developmental Characteristics of Longmaxi Formation Shaly Fissure in Changning of South of Sichuan Area. Science Technology & Engineering.
Warren, L.M., Shearer, P.M., 2000. Investigating the frequency dependence of mantle Q by stacking P and PP spectra. J. Geophys. Res. 105, 25391–25402. https://doi.org/10.1029/2000jb900283.
Wu, Q., Chapman, M., Chen, X., 2018. Stress-Drop variations of induced earthquakes in Oklahoma. Bull. Seismol. Soc. Am. 108, 1107–1123. https://doi.org/10.1785/0120170335.
Xie, X.B., 2005. Investigating explosion source energy partitioning and Lg-wave excitation using a finite-difference plus slowness analysis method. Bull. Seismol. Soc. Am. 95, 2412–2427. https://doi.org/10.1785/0120050023.
Yang, Y.-H., Hu, J.-C., Chen, Q., Lei, X., Zhao, J., Li, W., Xu, R., Chiu, C.-Y., 2021. Shallow slip of blind fault associated with the 2019 Ms 6.0 Changning earthquake in fold-and-thrust belt in salt mines of Southeast Sichuan, China. Geophys. J. Int. 224, 909–922. https://doi.org/10.1093/gji/ggaa488.
Yang, X., Li, Y., Ge, Z., Qiang, Z., 2022. Upper crustal anisotropy in the Southeastern Sichuan Basin, China from shear-wave splitting measurements. Tectonophysics. 837, 229431 https://doi.org/10.1016/j.tecto.2022.229431.
Yi, G.X., Long, F., Liang, M.J., Zhao, M., Wang, S.W., Gong, Y., Qiao, H.Z., Su, J.R., 2019. Focal mechanism solutions and seismogenic structure of the 17 June 2019 Ms6.0 Sichuan Changning earthquake sequence. Chin. J. Geophys. (in Chinese) 62 (9), 3432–3447. https://doi.org/10.6038/cjg2019N0297.
Zhang, Z.W., Cheng, W.Z., Wu, P., Gong, Y., Chen, W.K., Xu, Y., Zhou, X.Z., 2013. Study on earthquake relocation and P-wave velocity structure in the Zigong and Longchang area. Earthq. Res. China (in Chin.) 29 (1), 37–47. https://doi.org/10.3969/j.issn.1001-4683.2013.01.004.
Zhao, L.F., Mousavi, S.M., 2018. Lateral variation of crustal Lg attenuation in Eastern North America. Sci. Rep. 8, 7285. https://doi.org/10.1038/s41598-018-25649-5.
Zhao, L.F., Xie, X.B., Wang, W.M., Zhang, J.H., Yao, Z.X., 2010. Seismic Lg-wave Q tomography in and around Northeast China. J. Geophys. Res. 115, B08307. https://doi.org/10.1029/2009jb007157.
Zhao, L.F., Xie, X.B., He, J.K., Tian, X.B., Yao, Z.X., 2013a. Crustal flow pattern beneath the Tibetan Plateau constrained by regional Lg-wave Q tomography. Earth Planet. Sci. Lett. 383, 113–122. https://doi.org/10.1016/j.epsl.2013.09.038.
Zhao, L.F., Xie, X.B., Wang, W.M., Zhang, J.H., Yao, Z.X., 2013b. Crustal Lg attenuation within the North China Craton and its surrounding regions. Geophys. J. Int. 195, 513–531. https://doi.org/10.1093/gji/ggt235.
Zhao, L.F., Xie, X.B., Wang, W.M., Fan, N., Zhao, X., Yao, Z.X., 2017. The 9 September 2016 North Korean underground nuclear test. Bull. Seismol. Soc. Am. 107, 3044–3051. https://doi.org/10.1785/0120160355.
Zheng, X.-F., Ouyang, B., Zhang, D.-N., Yao, Z.-X., Liang, J.-H., Zheng, J., 2009. Technical system construction of data backup centre for China Seismograph Network and the data support to researches on the Wenchuan earthquake, *Chinese*. J. Geophys. (in Chin.) 100, 2866–2872. https://doi.org/10.1785/0120090257.